Neutron scattering off spherical nuclei with a global nonlocal dispersive optical model

B. Morillon,* G. Blanchon, and P. Romain
CEA, DAM, DIF, F-91297 Arpajon, France
and Université Paris-Saclay, CEA, LMCE, 91680 Bruyères-le-Châtel, France

H. F. Arellano
Department of Physics–FCFM, University of Chile, Avenida Blanco Encalada 2008, RM 8370449 Santiago, Chile
and CEA, DAM, DIF, F-91297 Arpajon, France

(Received 28 August 2023; accepted 13 March 2024; published 10 April 2024)

We present a global nonlocal and dispersive optical model potential for neutron scattering off spherical nuclei with incident energies up to 250 MeV. This optical model is an extension of the nondispersive Perey-Buck potential. The imaginary components are chosen to be energy dependent and the dispersive constraints are taken into account. The surface imaginary part is nonlocal, whereas the volume imaginary part above 10 MeV is local, allowing one to reproduce total cross sections and scattering data for high energies. We obtain a good description of scattering observables for target nuclei ranging from $A = 16$ up to 209. The inclusion of a nonlocal spin-orbit term enables a better description of the analyzing power data relative to the local dispersive model.

DOI: 10.1103/PhysRevC.109.044611

I. INTRODUCTION

More than fifteen years ago, two of us introduced a global local nucleon optical model potential (OMP) [1–3] including dispersion relations [4] and the local energy approximation of Perey and Buck [5]. This potential provides a good description of integral and differential elastic cross sections for neutron and proton scattering off spherical target nuclei for incident energy up to 250 MeV. Bound state energies were used as constraints for the calibration of the potential for neutrons [2] and protons [3]. The calibration of the parameters was made using the data set of Koning and Delaroche (KD) in Ref. [6], i.e., from mostly stable and spherical target nuclei. Based on the same method, Charity *et al.* have studied the evolution of the OMP for target nuclei with large proton-neutron asymmetry [7–9].

Since then, various attempts have been made to handle nonlocality explicitly. Tian *et al.* extended the Perey-Buck (PB) potential [5] to include both neutron and proton projectiles [10]. More recently, Mahzoon *et al.* proposed a dispersive nonlocal potential [11]. This potential has allowed for the first time the reproduction of the target density and the particle number of the target nucleus in addition to the usual scattering observables. First applied to ^{40}Ca for both neutron and proton projectiles, the approach has been extended to include ^{48}Ca [12] and ^{208}Pb [13]. In parallel, Lovell *et al.* [14] and Jaghoub *et al.* [15] have studied the energy dependence of nonlocal potentials. Those studies are all based on a PB separable potential which includes a Gaussian form factor for the nonlocality [5]. In a recent review, Hebborn *et al.* summarize efforts toward improvements, within both phenomenological and microscopic optical models approaches [16].

In this work, we present the first global dispersive and nonlocal OMP for neutron scattering off spherical target nuclei with incident energy up to 250 MeV. We adopt the PB form factor as the starting point. The imaginary contribution to the OMP is taken to be energy dependent whereas the real contribution is energy dependent only through the dispersion relation. Accounting for nonlocality enables us to get rid of spurious energy dependence stemming from local approximations. The calibration of the OMP parameters is done for 22 nuclei with masses ranging from $A = 16$ up to 209. Both experimental elastic scattering observables and bound state energies are considered in the calibration process.

We organize this work as follows. In Sec. II, we recall the basics of the Perey-Buck potential model. Then we contrast the predictive power of the two most common parametrizations: PB [5] and Tian, Pang, and Ma (TPM) [10]. In Sec. III, we present form factors for the real and imaginary components of the new nonlocal dispersive OMP. The resulting parameters of this OMP are presented and discussed in Sec. IV. Comparisons are made in Sec. V between calculated and experimental neutron cross sections, analyzing powers, and bound single-particle neutron states. Finally, in Sec. VII we present the main conclusions of this work. The method used to solve the integrodifferential Schrödinger equation is given in the Appendix.

II. PEREY-BUCK OPTICAL MODEL

In the early 1960s, Perey and Buck (PB) proposed a nonlocal phenomenological potential to describe neutron scattering off nuclei with incident energies below 28 MeV [5]. The

*benjamin.morillon@cea.fr

central part of the PB potential reads

$$V(\mathbf{r},\mathbf{r}') = U\left(\frac{|\mathbf{r}+\mathbf{r}'|}{2}\right)H(|\mathbf{r}-\mathbf{r}'|), \tag{1}$$

where H represents the nonlocality form factor, assumed to be Gaussian, which is given as

$$H(|\mathbf{r}-\mathbf{r}'|) = \frac{1}{\pi^{\frac{3}{2}}\beta^3}\exp\left[-\frac{(\mathbf{r}-\mathbf{r}')^2}{\beta^2}\right]. \tag{2}$$

Here β is the range of the nonlocality. The radial form factor U is given the Woods-Saxon form

$$U(\tilde{r}) = V_V f(\tilde{r},R,a) - iW_S 4a\frac{df(\tilde{r},R,a)}{d\tilde{r}}, \tag{3}$$

with f a two-parameter Fermi distribution given by

$$f(\tilde{r},R,a) = \frac{1}{1+e^{\frac{\tilde{r}-R}{a}}}. \tag{4}$$

Here $\tilde{r} = \frac{1}{2}|\mathbf{r}+\mathbf{r}'|$, a is the diffuseness parameter, and $R = r_0A^{1/3}$ is the target-nucleus radius, with r_0 the reduced radius and A the nucleus mass. Additionally the real volume strength V_V and the imaginary surface strength W_S are energy independent. No imaginary volume component was introduced by PB between 400 keV and 28 MeV. In addition, PB adopted a local prescription for the spin-orbit potential.

When dealing with nonlocal potentials, the scattering equations turn to be integrodifferential. One can express then scattering equations in partial waves,

$$\frac{\hbar^2}{2\mu}\left[\frac{d^2}{dr^2} - \frac{l(l+1)}{r^2}\right]u_{jl}(r) + Eu_{jl}(r) - V^{\mathrm{L}}_{jl}(r)u_{jl}(r) - \int_0^\infty v^{\mathrm{NL}}_{jl}(r,r')u_{jl}(r')dr' = 0, \tag{5}$$

with $u_{jl}(r)$ the radial wave function and μ the projectile-target reduced mass [17]. For the sake of completeness, we include both local and nonlocal contributions in Eq. (5). In the case of PB, the spin-orbit potential is local, where

$$V^{\mathrm{L}}_{jl}(r) = -[j(j+1) - l(l+1) - 3/4]U_{\mathrm{so}}(r), \tag{6}$$

which makes the local contribution (j,l) dependent. The form factors in Eqs. (1) and (2) allow for analytical expressions for the potential multipoles,

$$v^{\mathrm{NL}}_l(r,r') = \frac{4rr'}{\sqrt{\pi}\beta^3}U\left(\frac{r+r'}{2}\right)e^{-\frac{(r^2+r'^2)}{\beta^2}}i^l j_l\left(-i\frac{2rr'}{\beta^2}\right). \tag{7}$$

The method used to solve Eq. (5) is described in the Appendix.

In order to illustrate the predictive power of the PB potential, in Fig. 1 we plot experimental and calculated cross sections for ten target nuclei (Mg, Si, Ca, Cr, Y, Zr, Nb, Sn, Pb, Bi). Solid red and dashed blue curves denote results from PB and TPM parametrizations, respectively. The experimental total cross section has been averaged on the energy. The effect of this averaging is twofold. At low incident energies it filters out the compound nucleus contribution [18]. It also allows one to attenuate discrepancies coming from merging different data sets. In Fig. 2 we plot the experimental and calculated differential cross sections as functions of the scattering angle in the center-of-mass (c.m.) reference frame. For the sake of conciseness, we show only two angular distributions for each target nucleus. Here we include results for PB and TPM parametrizations adopting the same conventions as in Fig. 1.

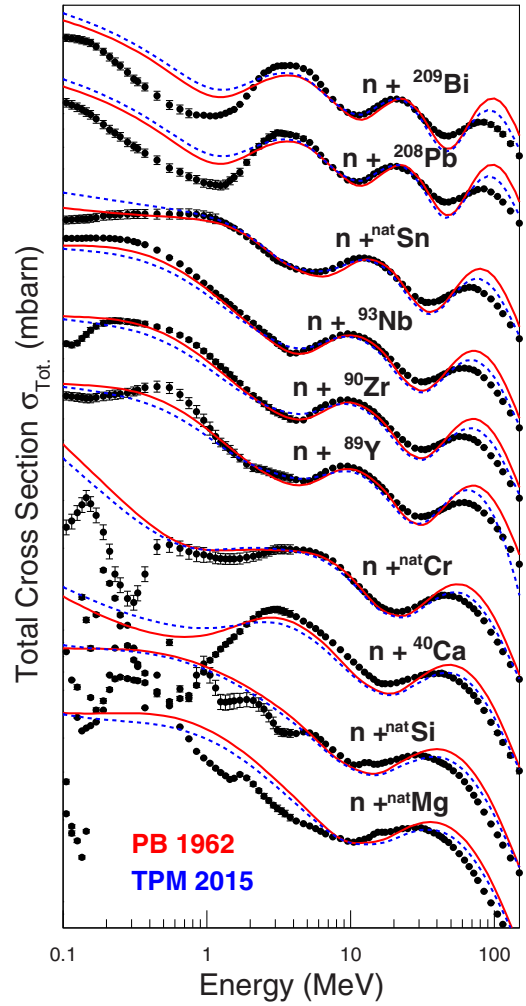

FIG. 1. Total cross section (in logarithmic scale) for neutron-nucleus scattering as functions of the beam energy. The data (symbols) are from Ref. [19]. Red solid curves correspond to the PB potential [5] and blue dashed curves to that of TPM [10].

While angular distributions are very well reproduced, the agreement for the total cross section is poor in the 0.4–28 MeV energy range for both parametrizations. It should be noted, however, that when Perey and Buck developed their potential in the early 1960s they did not have the current wealth of measurements. The TPM potential provides a better agreement for high-energy total cross sections. This is most likely due to the presence of a volume imaginary term in their parametrization. Note, however, that the experimental total cross section is systematically overestimated in the range 50–150 MeV.

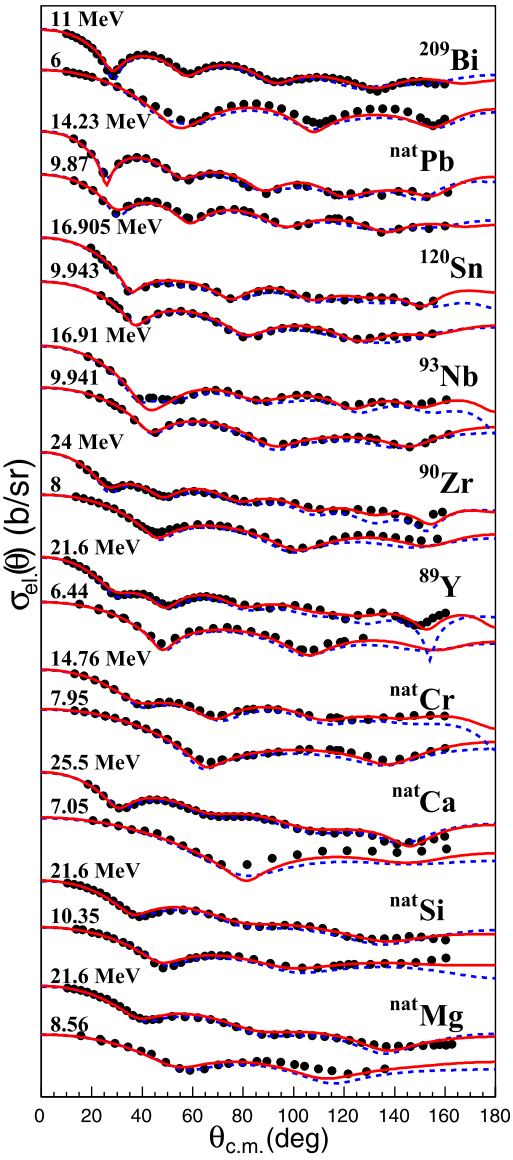

FIG. 2. Differential cross sections (in logarithmic scale) for neutron elastic scattering as functions of the c.m. scattering angle. Red solid curves correspond to the PB potential [5] while blue dashed curves denote TPM [10] results. Data are denoted by symbols [19].

III. NONLOCAL AND DISPERSIVE OPTICAL MODEL

Although neither microscopic nor *ab initio* approaches for nucleon-nucleus scattering are currently suited for massive and precise data evaluation, they can provide guidance to phenomenological models. On the other side, phenomenological approaches can become very useful mainly due to their simplicity and flexibility. The optical model potential is connected to microscopy through its correspondence with the self-energy [20]. The challenge here is to incorporate microscopic and *ab initio* features in the construction of phenomenological optical potentials.

One of these features is the nonlocality, emerging from the Pauli exclusion principle, in addition to dynamic polarization [21]. In a recent work it has been demonstrated that the nonlocality exhibits a bell shape [22]. These findings emerge from microscopic descriptions of nucleon-nucleus collisions based on density-dependent g-matrix folding model retaining nonlocalities at all stages [22,23]. It is found that the nonlocality form factor H [see Eq. (2)] is weakly energy dependent. The leading energy dependence takes place in the strengths of the potential. Moreover, the spin-orbit contribution results nonlocal. In the context of the PB approach [5], this nonlocality is modeled through a Gaussian form factor. We retain a single Gaussian nonlocality for real and imaginary components of the potential. As we will see, this is sufficient to achieve a reasonable description of experimental data.

Continuing the analogy with many-body physics, the optical potential can be separated into an energy-independent Hartree-Fock and energy-dependent polarization terms. Then, causality is ensured through a dispersion relation [24,25]. This dispersion relation relates scattering and bound-state properties. Hence, it allows one to determine scattering states and bound states of the target-nucleus on the same footing using a single potential. A well-constrained phenomenological nonlocal dispersive potential contains in practice all the correlations. Thus one can evaluate the quality of the microscopic description not only of scattering observables but also other physical properties such as occupation numbers, densities, and bound state energies.

A. Dispersion relation

The radial form factor U in Eq. (3) is now assumed to be energy dependent,

$$U(\tilde{r},E) = V(\tilde{r},E) + iW(\tilde{r},E), \tag{8}$$

whereas the nonlocal form factor H in Eq. (2) is kept energy independent. Now, a dispersion relation applies, relating the energy-dependent real and imaginary contributions in Eq. (8),

$$V(\tilde{r},E) = V_0(\tilde{r}) + \Delta V(\tilde{r},E),$$
$$\Delta V(\tilde{r},E) = \frac{\mathcal{P}}{\pi}\int_{-\infty}^{+\infty}\frac{W(\tilde{r},E')}{E'-E}dE', \tag{9}$$

where $\mathcal{P}$ denotes the principal value of the integral [4]. V_0 is an energy-independent potential often referred to as the Hartree-Fock potential [4], in analogy to the static self-energy in many-body physics [26]. When possible, the dispersive term ΔV is obtained analytically, otherwise it is calculated by numerical integration. We assume the energy dependence affects only the strengths of the potential. The diffuseness, radius, and nonlocality are assumed to be energy independent.

B. Real potentials

The real potential is assumed to be nonlocal, with a Gaussian nonlocal form factor H as in Eq. (2), and energy independent. Its radial form factor reads

$$V_0(\tilde{r}) = V_V^{\rm NL} f(\tilde{r},R,a) - V_S^{\rm NL} 4a\frac{df(\tilde{r},R,a)}{d\tilde{r}}$$
$$-2V_{\rm so}^{\rm NL}\left(\frac{\hbar}{m_\pi c}\right)^2\frac{1}{\tilde{r}}\frac{df(\tilde{r},R,a)}{d\tilde{r}}\,\mathbf{l}\cdot\mathbf{s}. \tag{10}$$

We include a real nonlocal surface potential $V_S^{\rm NL}$ that improves the agreement with the elastic angular distribution data. The spin-orbit potential is nonlocal with the same nonlocality as the central term. The dispersive component, $\Delta V(\tilde{r}, E)$, stemming from the energy-dependent imaginary potentials, is added as described in Eq. (9).

C. Imaginary potentials

As observed in Fig. 1, the addition of a volume imaginary contribution, as proposed by TPM [10], helps to better reproduce total cross section above 50 MeV. Following this prescription, we have tested several values of nonlocality parameters β for the volume imaginary potential. We have also investigated different energy dependencies. From these studies we conclude that a local volume imaginary potential is the best suited. The energy dependency retained for the volume and the surface terms are described below.

The local imaginary volume contribution reads

$$W^{\rm L}(r, E) = W_V^{\rm L}(E) f(r, R, a), \tag{11}$$

whereas the nonlocal imaginary surface contribution reads

$$W^{\rm NL}(\tilde{r}, E) = -W_S^{\rm NL}(E) 4a \frac{df(\tilde{r}, R, a)}{d\tilde{r}} - 2W_{\rm so}^{\rm NL}(E)\left(\frac{\hbar}{m_\pi c}\right)^2 \frac{1}{\tilde{r}} \frac{df(\tilde{r}, R, a)}{d\tilde{r}} \mathbf{l}\cdot\mathbf{s}. \tag{12}$$

It should be noted that the imaginary spin-orbit is chosen to be nonlocal.

1. Surface imaginary depth

For the depth of the nonlocal imaginary surface strength, we use a Brown-Rho shape [27] modified by an exponential falloff,

$$W_S^{\rm NL}(E) = A_S^{\pm}(E - E_F)^n \frac{\exp(-C_S|E - E_F|)}{(E - E_F)^n + B_S^n}. \tag{13}$$

Its energy dependence is asymmetric with respect to the neutron Fermi energy $E_F = -[S_n(Z, N) - S_n(Z, N + 1)]/2$. There is a single depth value A_S^+ for $E > E_F$, and another one A_S^- for $E < E_F$. We have investigated different values for the parameter n, reaching better fits with $n = 2$. We also found that coefficients A_S^-, B_S, and C_S exhibit a very weak dependence on target-nucleus mass, so that it is reasonable to assume them constant. In contrast, A_S^+ decreases linearly with respect to the mass A.

2. Volume imaginary depth

For energies around the Fermi energy, within the interval $[E_F - E_V^-, E_F + E_V^+]$, the depth of the local imaginary volume component is of Brown-Rho type [27] but with different depths $A_V^{\pm}$, depending on whether the projectile energy is above (A_V^+) or below (A_V^-) the Fermi energy, namely

$$W_V^{\rm L}(E) = \frac{A_V^{\pm}(E - E_F)^2}{(E - E_F)^2 + B_V^2}. \tag{14}$$

TABLE I. Energy and mass dependency of real and imaginary potential strengths.

Nonlocal real depth	
$V_V^{\rm NL}$ (MeV)	$-69.71 - 1.140 \times 10^{-2}A$
$V_S^{\rm NL}$ (MeV)	$-8.600 - 8.000 \times 10^{-3}A$
$V_{\rm so}^{\rm NL}$ (MeV)	$-9.787 - 1.140 \times 10^{-2}A$
Nonlocal surface imaginary depth	
$W_S^{\rm NL}(E) = A_S^{\pm}(E - E_F)^2 \frac{\exp(-C_S\lvert E - E_F\rvert)}{(E - E_F)^2 + B_S^2}$	
A_S^+ (MeV)	$-19.62 - 1.500 \times 10^{-2}A$ for $E_F < E$
A_S^- (MeV)	-16.00 for $E < E_F$
B_S (MeV)	11.11
C_S (MeV^{-1})	9.200×10^{-3}
Local volume imaginary depth	
For $E > E_F + E_V^+$:	
$W_V^{\rm L}(E) = \frac{A_V^+(E - E_F)^2}{(E - E_F)^2 + B_V^2} + \alpha(\sqrt{E} + \frac{(E_F + E_V^+)^{3/2}}{2E} - \frac{3}{2}\sqrt{E_F + E_V^+})$.	
For $E_F - E_V^- < E < E_F + E_V^+$:	
$W_V^{\rm L}(E) = \frac{A_V^{\pm}(E - E_F)^2}{(E - E_F)^2 + B_V^2}$.	
For $E < E_F - E_V^-$:	
$W_V^{\rm L}(E) = \frac{A_V^-(E - E_F)^2}{(E - E_F)^2 + B_V^2}\left(1 - \frac{(E - E_F + E_V^-)^2}{(E - E_F + E_V^-)^2 + (E_V^-)^2}\right)$	
with	
A_V^+ (MeV)	$-32.40 - 2.000 \times 10^{-2}A$ for $E > E_F$
A_V^- (MeV)	$-8.400A$ for $E < E_F$
B_V (MeV)	135.0
E_V^+ (MeV)	$40.00 - 9.000 \times 10^{-2}A$
E_V^- (MeV)	25.50
α (MeV$^{1/2}$)	$3.000 \times 10^{-1} + 2.000 \times 10^{-3}A$
Nonlocal spin-orbit imaginary depth	
$W_{\rm so}^{\rm NL}(E) = \frac{A_{\rm so}(E - E_F)^2}{(E - E_F)^2 + C_{\rm so}^2} - \frac{B_{\rm so}(E - E_F)^2}{(E - E_F)^2 + D_{\rm so}^2}$	
$A_{\rm so}$ (MeV)	4.893
$B_{\rm so}$ (MeV)	2.447
$C_{\rm so}$ (MeV)	50.00
$D_{\rm so}$ (MeV)	3.900

For energies E above $E_F + E_V^+$, the form proposed by Mahaux and Sartor [4] is applied, thus

$$W_V^{\rm L}(E) = \frac{A_V^+(E - E_F)^2}{(E - E_F)^2 + B_V^2} + \alpha\left[\sqrt{E} + \frac{(E_F + E_V^+)^{3/2}}{2E} - \frac{3}{2}\sqrt{E_F + E_V^+}\right]. \tag{15}$$

In the case of E below $E_F - E_V^-$, the strength is given by

$$W_V^{\rm L}(E) = \frac{A_V^-(E - E_F)^2}{(E - E_F)^2 + B_V^2} \times \left[1 - \frac{(E - E_F + E_V^-)^2}{(E - E_F + E_V^-)^2 + (E_V^-)^2}\right]. \tag{16}$$

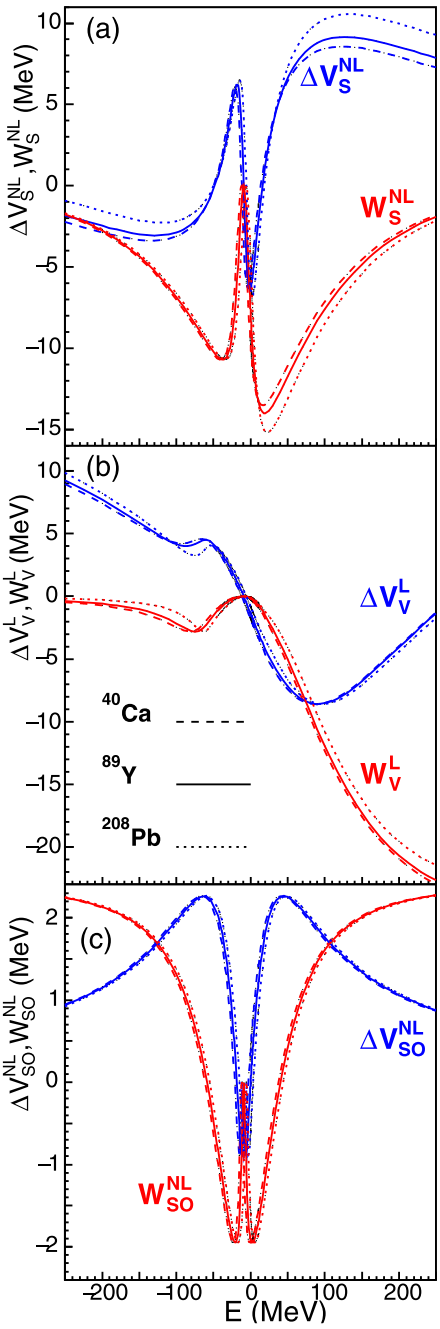

FIG. 3. Depths W (red curve) and dispersive contribution ΔV of surface (a), volume (b), and spin-orbit (c) imaginary potentials as functions of the energy. Dashed, solid, and dotted curves denote results for ^{40}Ca, ^{89}Y, and ^{208}Pb, respectively.

3. Spin-orbit imaginary depth

For the spin orbit term, the imaginary surface strength is taken to be symmetrical with respect to the Fermi energy. It reads

$$W_{so}^{NL}(E) = \frac{A_{so}(E-E_F)^2}{(E-E_F)^2+C_{so}^2} - \frac{B_{so}(E-E_F)^2}{(E-E_F)^2+D_{so}^2}, \quad (17)$$

consisting of the difference of two Brown-Rho forms, allowing an analytical expression for the dispersive term $\Delta V_{so}^{NL}(E)$ [28].

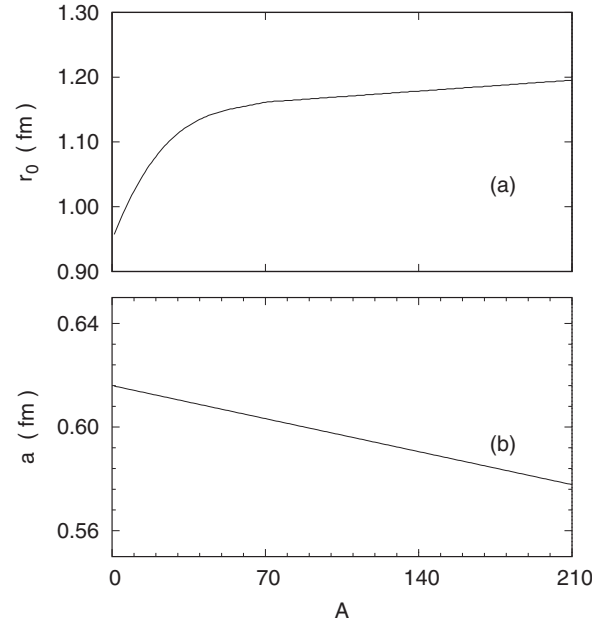

FIG. 4. Reduced radius r_0 (a) and diffuseness a (b) as functions of the target mass A for the nonlocal dispersive model.

IV. PARAMETER CALIBRATION

Once the potential form factors are specified, we look for the parameters that best reproduce the experimental data. For each nucleus we carry out an iterative parameter calibration to minimize the difference between data and the nonlocal dispersive optical model results. Then one can identify the dependence of the parameters on the nucleus mass A and the energy. The variation of the parameters with respect to the mass and the energy is expected to be smooth, helping the model to gain predictive power. This parameter search is highly time consuming, necessitating the use of parallel computing. For each nucleus, over 2000 processors are used for twenty-four hours to find the parameters. In addition, for low neutron energy (below about 15 MeV), compound neutron emission is described with the Hauser-Feshbach formalism [29] using NLD transmission coefficients in TALYS code [30]. This process is accounted for in the calibration process.

Our search procedure makes extensive use of the comprehensive EXFOR database [19]. In the energy range from 1 keV to 250 MeV, the experimental data of the following 22 elements are used to determine our parameters: C, O, Mg, Al, Si, S, Ca, Ti, Cr, Fe, Ni, Cu, Y, Zr, Nb, Mo, Sn, Ce, Au, Hg, Pb, Bi. About 100 energy points are needed to describe accurately the variations of the total cross section in the energy range from 1 keV to 250 MeV. As already mentioned, for neutron energies below a few MeV and especially for light nuclei, the experimental total cross section must be averaged because of the presence of compound nucleus resonances. This averaged total cross section (see Fig. 1) is retained throughout the calibration. After each step of parameter search, we calculate bound state energies as well as analyzing powers.

TABLE II. Nonlocality and mass dependence of depth, radii, and diffuseness of NLD potential.

Geometrical parameters	
r_0 $(70 < A)$ (fm)	$1.1446 + 2.4200 \times 10^{-4}A$
r_0 $(A < 70)$ (fm)	$9.4860 \times 10^{-1} + 8.8000 \times 10^{-3}A$
	$-1.3200 \times 10^{-4}A^2 + 7.1000 \times 10^{-7}A^3$
a (fm)	$6.1600 \times 10^{-1} - 1.8200 \times 10^{-4}A$
β (fm)	0.915

The resulting parameters for strengths of the real and imaginary potentials are summarized in Table I. In Fig. 3, we present the strengths of the surface [panel (a)], volume [panel (b)] and spin-orbit [panel (c)] imaginary contributions (red curves) together with their respective dispersive contributions (blue curves) for three target-nuclei: ^{40}Ca, ^{89}Y, and ^{208}Pb. In panel (a), $W_S^{\rm NL}$ is nonsymmetrical with respect to the Fermi energy. This asymmetry results from the fact that the phase space of particle levels for $E \ll E_F$ is significantly larger than that of hole levels for $E \gg E_F$. Therefore the contributions from two-particle–one-hole states for $E \ll E_F$ will be larger than that for two-hole–one-particle states at $E \gg E_F$ [8]. In panel (c), $W_{\rm so}^{\rm NL}$ is independent of the mass and symmetrical with respect to the Fermi energy. The real depths of the volume surface and spin-orbit potential ($V_V^{\rm NL}$, $V_S^{\rm NL}$, and $V_{\rm so}^{\rm NL}$) are independent of the energy of the projectile. The variations as a function of the mass of the nuclei are weak for the surface and volume depths, as shown in Table I.

The optimum nonlocality range β is found to be 0.915 fm, larger than in previous works [5,10]. The same radius and diffuseness are used for real and imaginary contributions. In Fig. 4 we plot the reduced radius r_0 [panel (a)] and the diffuseness a [panel (b)] as functions of the mass A. The reduced radius increases with mass in contrast to diffuseness, which is a linear function decreasing as the mass increases. For the former, the variation is linear for masses greater than 70, while for smaller masses the expression of the radius behaves as a polynomial of degree 3. Results are summarized in Table II.

V. COMPARISON BETWEEN LOCAL AND NONLOCAL DISPERSIVE MODELS

We examine differences in the calculated scattering observables for neutron scattering as implied by the local dispersive (LD) model of Ref. [3] and the nonlocal dispersive (NLD) model presented in this work.

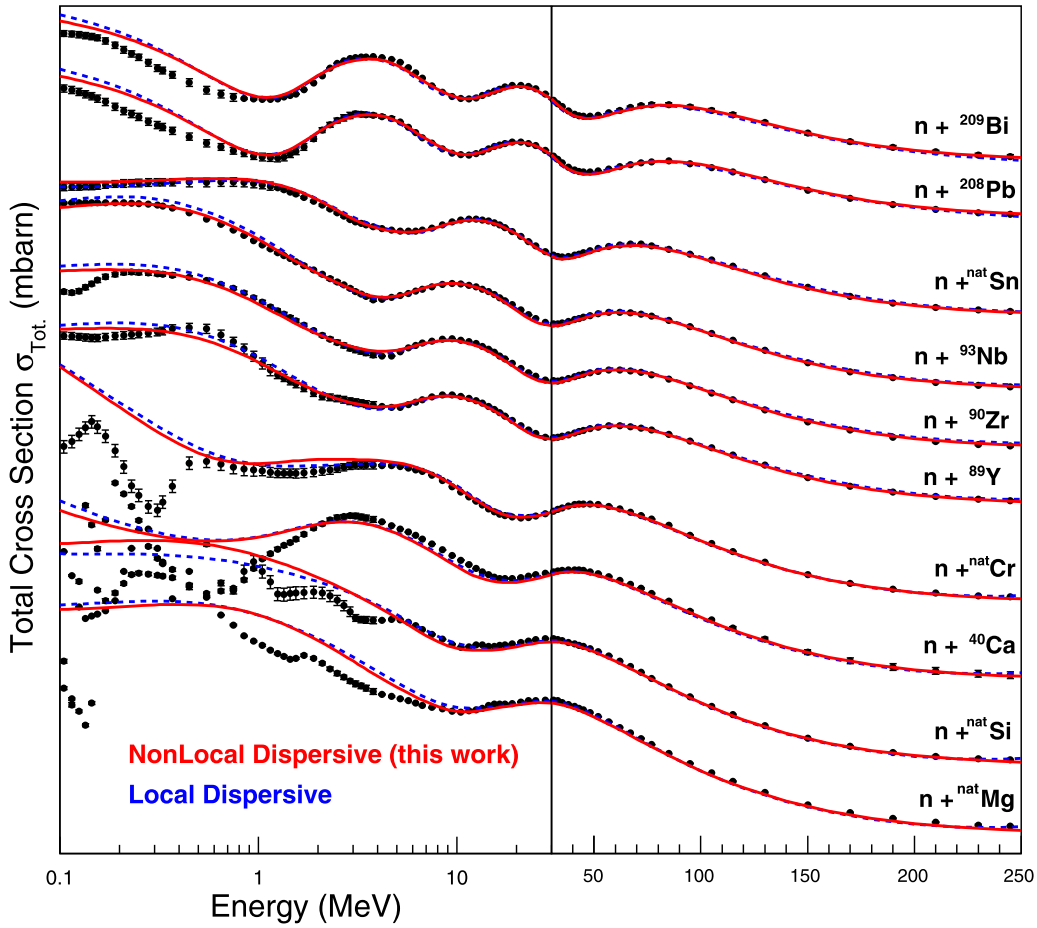

FIG. 5. Total cross section for neutron-nucleus scattering as function of the energy. The data (symbols) are from Ref. [19]. Red solid curves correspond to NLD potential (this work) and blue dashed curves to LD potential [3].

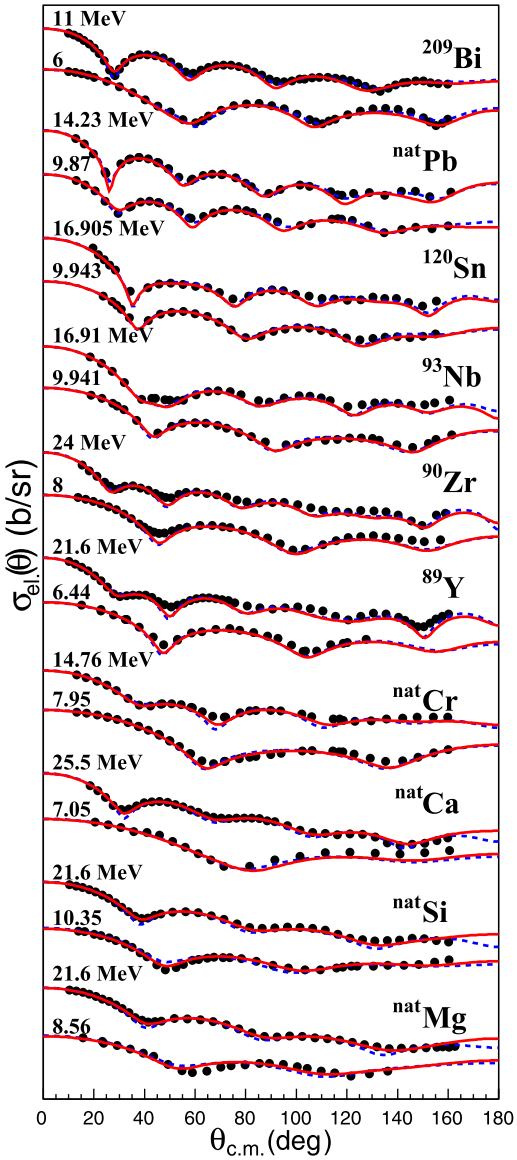

FIG. 6. Differential cross sections (in logarithmic scale) for neutron elastic scattering. Data are denoted by symbols [19]. Red solid curves correspond to NLD potential (this work) and blue dashed curves to LD potential [3].

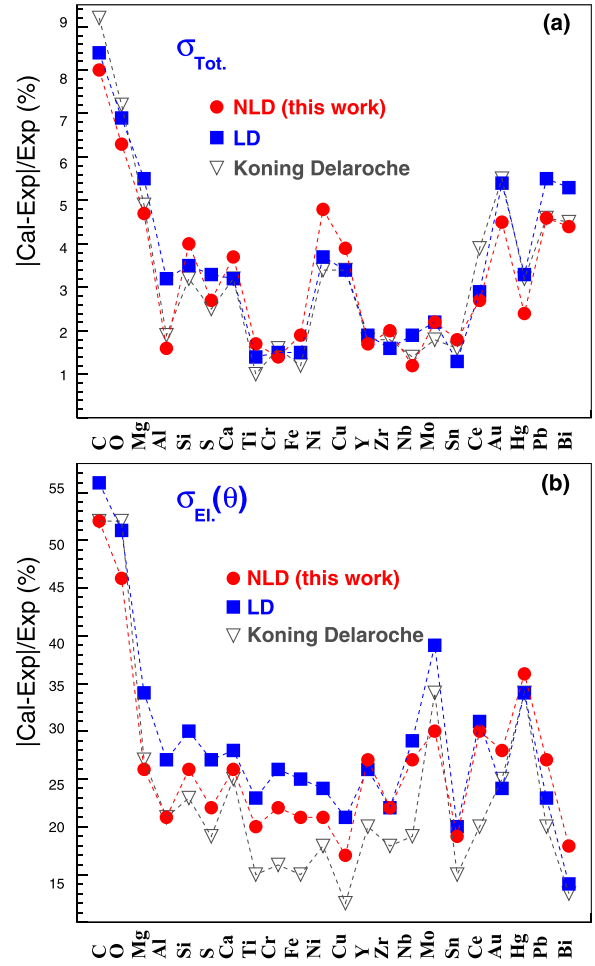

FIG. 7. Relative differences experimental vs calculation expressed as percentages for each nucleus (dashed curves) for total cross section (a) and differential cross section (b). Results are for NLD potentials (red circles), LD potential [3] (blue square), and KD potential [6] (black triangle).

In Fig. 5 we plot the total cross sections for neutron-nucleus scattering as function of energy. We include ten targets with masses between 24 and 209. Dashed blue curves denote results from LD model whereas solid red curves denote NLD results (this work). We observe that the models yield comparable results for σ_T for neutron energies above $\approx$10 MeV. Differences are evident at lower energies, although the models' agreements with the data are comparable.

In Fig. 6 we show results for the differential cross section as a function of the scattering angle in the center-of-mass reference frame ($\theta_{c.m.}$). The targets we include in this case are the same as in Fig. 5, with neutron energies ranging from 6 up to 25.5 MeV. Although the angular descriptions of the data appear comparable between NLD and LD models, some differences are evident in their maxima and minima, with the NLD approach being in closer agreement with the data.

To compare the agreements with the data of NLD and LD approaches, we have calculated relative differences with the data for all the cases considered in the fit procedure. Results for these differences are shown in Fig. 7, where panel (a) summarizes results for the total cross section and panel (b) summarizes those for the differential cross section. Red circles (blue squares) denote results from NLD (LD) approaches. Additionally, as a reference, we include in this analysis the KD non-dispersive model (black triangles). From panel (a) we observe that all three models yield comparable agreements in σ_T, of the order of 3% for medium-mass nuclei. However, for light nuclei the NLD model yields better agreement (by roughly $\approx$1 %) relative to the LD approach. In the case of the differential cross section, panel (b) of Fig. 7 shows that the NLD approach is in better agreement with the data relative to the LD model, particularly for all targets with nuclear masses below 64. In Fig. 8 we show the analyzing powers (red curves) obtained from our nonlocal OMP for two incident

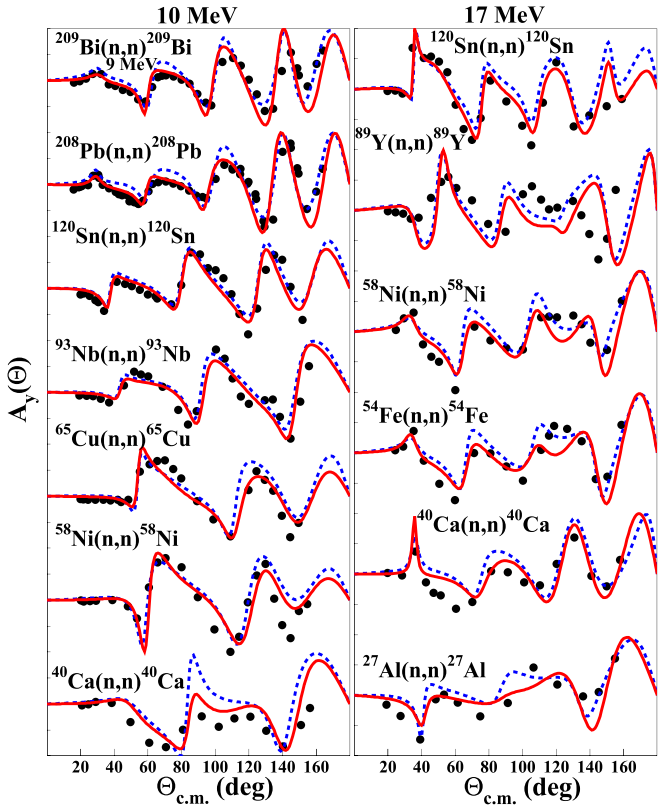

FIG. 8. Analyzing powers (in linear scale) for neutron scattering at 10 and 17 MeV. Data are denoted by symbols. Red solid curves are obtained with NLD potential and the blue dashed curves with LD potential.

neutron energies (10 and 17 MeV) with the following nuclei: ^{27}Al, ^{40}Ca, ^{54}Fe, ^{58}Ni, ^{65}Cu, ^{89}Y, ^{93}Nb, ^{120}Sn, ^{208}Pb, and ^{209}Bi. These results are compared with those calculated with the LD potential (blue dashed curves). This figure shows that the nonlocal potential better reproduces the analyzing powers, particularly their maxima and minima.

In Fig. 9 we show the experimental and calculated neutron single-particle energies for ^{208}Pb, ^{90}Zr, and ^{40}Ca. We include results from LD and NLD global potentials. We observe comparable agreements of these two models with the data, leaving room for improvement.

VI. UNCERTAINTIES

To assess the effect of random variations of the parameters of the NLD model on scattering observables, we have calculated the standard deviation for the calculated cross sections when geometrical parameters and strengths are varied. Specifically, in Fig. 10 we show the calculated elastic σ_E (blue curves), reaction σ_R (black curves), and total σ_T (red curves) cross sections for $n + ^{208}$Pb elastic scattering between 1 keV and 250 MeV. In this case, at each energy we allowed uniform variations for radius (1%), diffuseness (4%), real volume and surface depth (2%), and range of nonlocality (2%). Additionally, we allow for 20% variations of the depth of the imaginary terms. Thus, we performed stratified samplings of parameters over a uniform distribution, resulting in 2000 sets of parameters $(r, a, V_S, V_V, \beta, W_S, W_V)$, each of them leading to values for σ_E, σ_R, and σ_T. In Fig. 10 we plot the mean value (solid curves) together with its $\pm 1\sigma$ variations (shaded areas). It is interesting to note that, for energies above 0.2 MeV, the cross sections suffer rather moderate variations under variations of parameters. Therefore, the limitations of the model shown in Fig. 5 for σ_T can be attributed not to the parameters but to the assumed structure in the separable construction. This is an indication that a more complete model is needed.

VII. CONCLUSIONS

We have presented the first global, nonlocal, and dispersive optical model potential for neutron elastic scattering off spherical nuclei. The model is suited for beam energies up to 250 MeV and for target masses $16 \leqslant A \leqslant 209$. Both central and spin-orbit terms include a nonlocal Gaussian form factor of Perey-Buck type. Additionally, the imaginary volume potential includes a local term. The strengths of the model are constrained by dispersion relations, allowing a good description of integrated and angular scattering data. The dispersion relation allows one to determine scattering states and bound states of the target nucleus with a single potential. We are fully aware that there remains room for improvement for the description of bound state properties. We obtain a better description of the angular scattering data for $A \lesssim 65$ relative to the LD approach [3]. These improvements appear more evident in the analyzing power, suggesting the relevance of nonlocality in the spin-orbit term. This finding is in line with microscopic studies of nonlocality [22], where both central and spin-orbit components are nonlocal. As already mentioned, an important advantage of global phenomenological approaches for nucleon scattering lies on their simplicity, making feasible computations which would require physical information on processes involving the whole nuclear chart and over a broad energy range. The challenge in this approach is to identify strengths and form factors as implied from more fundamental approaches such as microscopic [31–34] or *ab initio* [35–37] ones. Efforts along this line are under way.

ACKNOWLEDGMENTS

This work was performed using HPC resources from CCRT. H.F.A. thanks the hospitality of colleagues of CEA, DAM, DIF during his stay at Bruyères-le-Châtel.

APPENDIX: RESOLUTION OF THE INTEGRODIFFERENTIAL SCHRÖDINGER EQUATION

The search procedure for strengths and geometrical parameters implies comparisons between data and scattering observables resulting from the nonlocal optical model we have discussed. This requires solving the integrodifferential Schrödinger equation (5) for several targets, energies, and varying parameters. Thus, we need a fast and accurate method to obtain the scattering wave functions. Along this line, Eq. (5) is solved by expanding u_{jl} on the Chebyshev polynomial basis. Since these polynomials are defined in the interval $[-1, +1]$ we use the new variable $x = \frac{2}{R_M} r - 1$. The quantity R_M represents the maximum value of the variable r (it defines

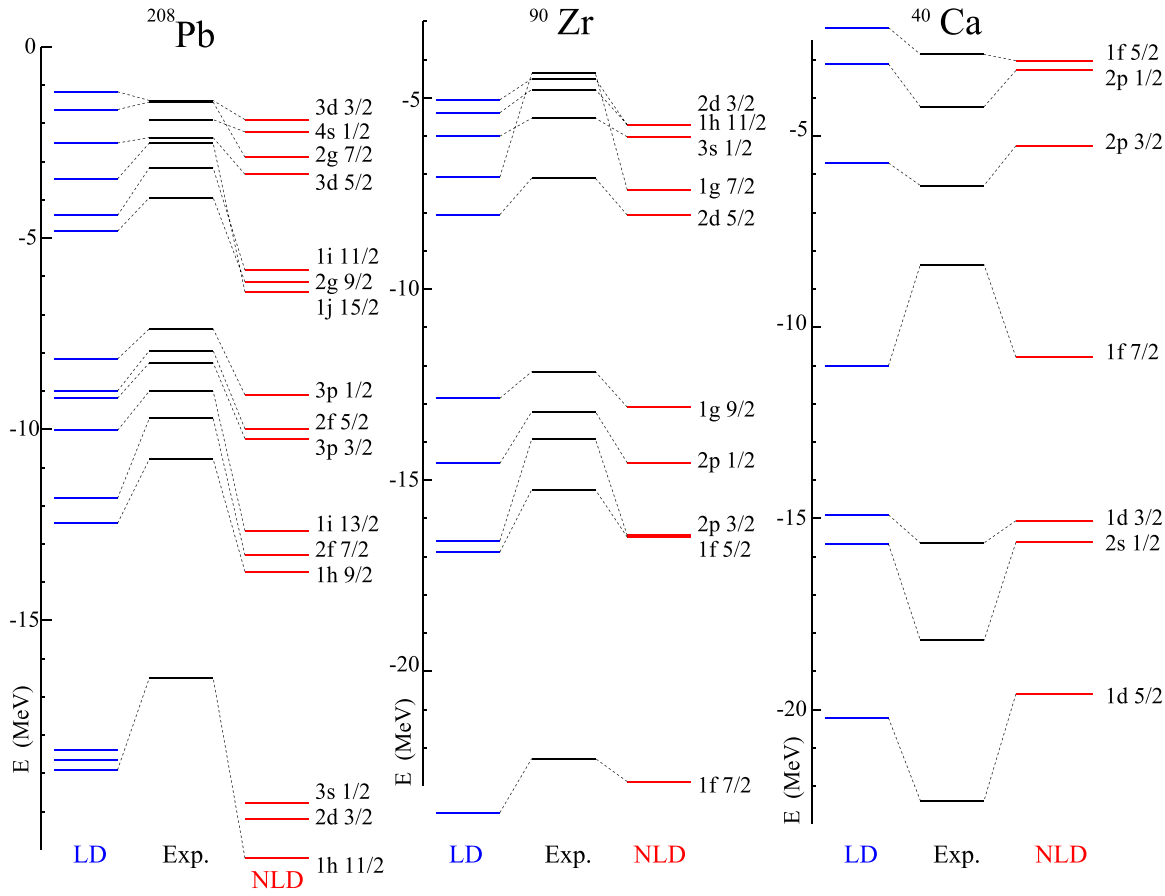

FIG. 9. Neutron single-particle energies for ^{208}Pb, ^{90}Zr, and ^{40}Ca determined with LD and NLD potentials and from experiment.

the radius where the potential becomes negligible). Thus the radial wave function u is written as a linear combination of N Chebyshev polynomials T_k weighted by the coefficients C_k. It reads

$$u\left[\frac{R_M}{2}(x+1)\right] \simeq \sum_{k=0}^{N-1}{}' C_k T_k(x), \quad x \in [-1,+1], \quad \text{(A1)}$$

where the symbol $'$ indicates that the first term of the sum is divided by a factor of 2, following the notation of Masson and Handscomb [38].

To obtain the radial part of the wave function we need to find the coefficients C_k with $k = 0, \ldots, N-1$. That is, we need N equations. The boundary conditions at $r = 0$ and $r = R_M$, yield two equations. Then, considering that $T_k(1) = 1$ and $T_k(-1) = (-1)^k$, we get

$$u(r=0) = \sum_{k=0}^{N-1}{}' (-1)^k C_k = 0, \quad \text{(A2)}$$

$$u(r=R_M) = \sum_{k=0}^{N-1}{}' C_k = 1 + i, \quad \text{(A3)}$$

where $1 + i$ is an arbitrary boundary value with no impact on the calculated phase shift [17]. It thus remains to find $N-2$ equations in order to determine the C_k coefficients. This is done by evaluating Eq. (5) at each of the $N-2$ roots x_n of

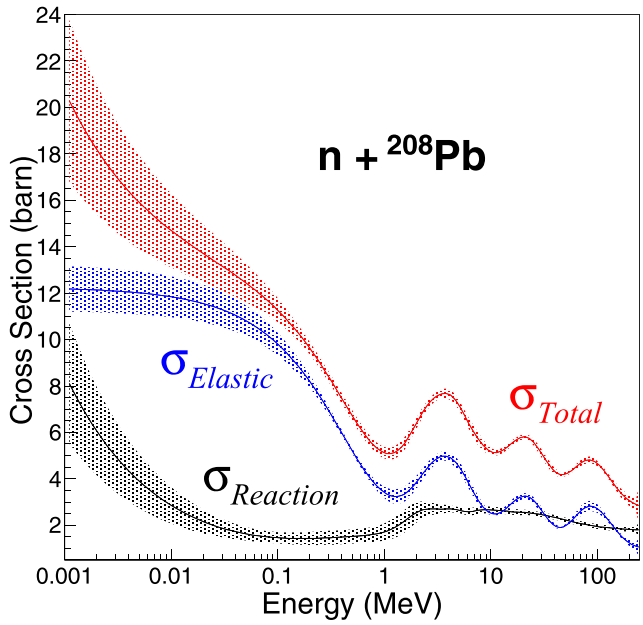

FIG. 10. Uncertainties ($\pm 1\sigma$) in the total (red), reaction (black) and elastic (blue) cross sections for neutron scattering of ^{208}Pb.

the T_{N-2} Chebyshev polynomial. These roots are

$$x_n = \cos\frac{(n-1/2)\pi}{N-2}, \quad n = 1,\ldots,N-2. \tag{A4}$$

In the case of the second derivative of the radial part of the wave function, we take advantage of the second derivative of the Chebyshev polynomials,

$$\left.\frac{d^2u\left(\frac{R_M}{2}(x+1)\right)}{dx^2}\right|_{x=x_n} = \sum_{k=2}^{N-1} C_k \sum_{\substack{m=0 \\ m-r \text{ even}}}^{k-2}{}' (k-m)k(k+m)T_m(x_n). \tag{A5}$$

In the case of a local potential, where we denote

$$\mathcal{V}^{\mathrm{L}}(r) = \frac{l(l+1)}{r^2} + \frac{2\mu}{\hbar^2}V(r), \tag{A6}$$

the $N-2$ equations representing Eq. (5) become

$$\frac{4}{R_M^2}\sum_{k=2}^{N-1} C_k \sum_{\substack{m=0 \\ k-m \text{ even}}}^{k-2}{}' (k-m)k(k+m)T_m(x_n) + \sum_{k=0}^{N-1}{}' C_k T_k(x_n)\left[\frac{2\mu E}{\hbar^2} - \mathcal{V}^{\mathrm{L}}\left(\frac{R_M}{2}(x_n+1)\right)\right] = 0. \tag{A7}$$

When a nonlocal potential is considered, an additional development taking advantage of the Chebyshev basis is pursued. As for the local potential, the nonlocal potential is also redefined as

$$\mathcal{V}^{\mathrm{NL}}(r,r') = \frac{2\mu}{\hbar^2}V(r,r'), \tag{A8}$$

and the term

$$-\frac{R_M}{2}\int_{-1}^{+1}\mathcal{V}^{\mathrm{NL}}\left[\frac{R_M}{2}(x_n+1), \frac{R_M}{2}(y+1)\right]u\left[\frac{R_M}{2}(y+1)\right]dy, \tag{A9}$$

must be added to Eq. (A7) to obtain a Schrödinger equation with local and nonlocal potentials. In order to perform the integration, the potential is expressed in terms of Chebyshev polynomials. This development concerns the variable y of this potential:

$$\mathcal{V}^{\mathrm{NL}}\left[\frac{R_M}{2}(x+1), \frac{R_M}{2}(y+1)\right] \simeq \sum_{m=0}^{M}{}' v_m\left[\frac{R_M}{2}(x+1)\right]T_m(y). \tag{A10}$$

The v_m terms are obtained by considering the $M+1$ zeros of the Chebyshev polynomial T_{M+1},

$$y_p = \cos\frac{(p-1/2)\pi}{M+1}, \quad p = 1,\ldots,M+1, \tag{A11}$$

and, using the discrete orthogonality relations [38], one obtains the v_m terms

$$\begin{aligned}\sum_{p=1}^{M+1}\mathcal{V}^{\mathrm{NL}}\left[\frac{R_M}{2}(x+1), \frac{R_M}{2}(y_p+1)\right]T_m(y_p) &= \sum_{p=1}^{M+1}\sum_{i=0}^{M}{}' v_i\left[\frac{R_M}{2}(x+1)\right]T_i(y_p)T_m(y_p) \\ &= \frac{M+1}{2}v_m\left[\frac{R_M}{2}(x+1)\right].\end{aligned} \tag{A12}$$

The calculation of the integral in Eq. (A9) is thus reduced to a sum:

$$\begin{aligned}&\int_{-1}^{+1}\sum_{m=0}^{M}{}' v_m\left[\frac{R_M}{2}(x+1)\right]T_m(y)\sum_{k=0}^{N-1}{}' C_k T_k(y)dy \\ &= \sum_{m=0}^{M}{}' v_m\left[\frac{R_M}{2}(x+1)\right]\sum_{k=0}^{N-1}{}' C_k\int_{-1}^{+1}T_m(y)T_k(y)dy \\ &= -2\sum_{k=0}^{N-1}{}' C_k\sum_{m=0}^{M}{}' v_m\left[\frac{R_M}{2}(x+1)\right] \\ &\quad\times\left.\frac{m^2+k^2-1}{(m^2+k^2-1)^2-4m^2k^2}\right|_{m+k \text{ even}}.\end{aligned} \tag{A13}$$

The $N-2$ equations needed to determine the coefficients C_k with local and nonlocal potentials are therefore written, with $n = 1,\ldots,N-2$,

$$\begin{aligned}&\frac{4}{R_M^2}\sum_{k=2}^{N-1} C_k \sum_{\substack{m=0 \\ k-m \text{ even}}}^{k-2}{}' (k-m)k(k+m)T_m(x_n) \\ &+ R_M\sum_{k=0}^{N-1}{}' C_k\sum_{m=0}^{M}{}' v_m\left(\frac{R_M}{2}(x_n+1)\right) \\ &\times\left.\frac{m^2+k^2-1}{(m^2+k^2-1)^2-4m^2k^2}\right|_{m+k \text{ even}} \\ &+\sum_{k=0}^{N-1}{}' C_k T_k(x_n)\left(\frac{2\mu E}{\hbar^2} - \mathcal{V}^{\mathrm{L}}\left(\frac{R_M}{2}(x_n+1)\right)\right) = 0.\end{aligned} \tag{A14}$$

The C_k coefficients with $k = 0,\ldots,N-1$ are calculated by solving a system of N linear equations using the lower-upper (LU) decomposition algorithm [39]. The function has been modified to allow calculation with complex numbers. Since the energy-dependent part of the phenomenological potential is separated from the spatial part, the decomposition of the potential on the Chebyshev polynomials needs to be performed only once for each nucleus. Up to 100 MeV, 30 Chebyshev polynomials are sufficient to accurately describe the wave function. Up to 250 MeV, the function must be developed using over 50 polynomials.

[1] B. Morillon and P. Romain, Phys. Rev. C **70**, 014601 (2004).
[2] B. Morillon and P. Romain, Phys. Rev. C **74**, 014601 (2006).
[3] B. Morillon and P. Romain, Phys. Rev. C **76**, 044601 (2007).
[4] C. Mahaux and R. Sartor, *Advances in Nuclear Physics*, edited by J. W. Negele and E. Vogt (Springer, Boston, MA, 1991), pp. 1–223.
[5] F. Perey and B. Buck, Nucl. Phys. **32**, 353 (1962).
[6] A. J. Koning and J.-P. Delaroche, Nucl. Phys. A **713**, 231 (2003).
[7] R. J. Charity, L. G. Sobotka, and W. H. Dickhoff, Phys. Rev. Lett. **97**, 162503 (2006).
[8] R. J. Charity, J. M. Mueller, L. G. Sobotka, and W. H. Dickhoff, Phys. Rev. C **76**, 044314 (2007).
[9] J. M. Mueller, R. J. Charity, R. Shane, L. G. Sobotka, S. J. Waldecker, W. H. Dickhoff, A. S. Crowell, J. H. Esterline, B. Fallin, C. R. Howell *et al.*, Phys. Rev. C **83**, 064605 (2011).
[10] Y. Tian, D.-Y. Pang, and Z.-Y. Ma, Int. J. Mod. Phys. E **24**, 1550006 (2015).
[11] M. H. Mahzoon, R. J. Charity, W. H. Dickhoff, H. Dussan, and S. J. Waldecker, Phys. Rev. Lett. **112**, 162503 (2014).
[12] M. H. Mahzoon, M. C. Atkinson, R. J. Charity, and W. H. Dickhoff, Phys. Rev. Lett. **119**, 222503 (2017).
[13] M. C. Atkinson, W. H. Dickhoff, M. Piarulli, A. Rios, and R. B. Wiringa, Phys. Rev. C **102**, 044333 (2020).
[14] M. I. Jaghoub, A. E. Lovell, and F. M. Nunes, Phys. Rev. C **98**, 024609 (2018).
[15] A. E. Lovell, P.-L. Bacq, P. Capel, F. M. Nunes, and L. J. Titus, Phys. Rev. C **96**, 051601(R) (2017).
[16] C. Hebborn, F. M. Nunes, G. Potel, W. H. Dickhoff, J. W. Holt, M. C. Atkinson, R. B. Baker, C. Barbieri, G. Blanchon, M. Burrows *et al.*, J. Phys. G: Nucl. Part. Phys. **50**, 060501 (2023).
[17] C. J. Joachain, *Quantum Collision Theory* (North-Holland, Amsterdam, 1975).
[18] H. Feshbach, C. E. Porter, and V. F. Weisskopf, Phys. Rev. **96**, 448 (1954).
[19] N. Otuka, E. Dupont, V. Semkova, B. Pritychenko, A. Blokhin, M. Aikawa, S. Babykina, M. Bossant, G. Chen, S. Dunaeva *et al.*, Nucl. Data Sheets **120**, 272 (2014).
[20] J. S. Bell and E. J. Squires, Phys. Rev. Lett. **3**, 96 (1959).
[21] P. Fraser, K. Amos, S. Karataglidis, L. Canton, G. Pisent, and J. P. Svenne, Eur. Phys. J. A **35**, 69 (2008).
[22] H. F. Arellano and G. Blanchon, Eur. Phys. J. A **58**, 119 (2022).
[23] H. F. Arellano and G. Blanchon, Comput. Phys. Commun. **259**, 107543 (2021).
[24] C. Mahaux, H. Ngô, and G. Satchler, Nucl. Phys. A **449**, 354 (1986).
[25] M. H. Mahzoon, Ph.D. thesis, Washington University in St. Louis, 2015 (unpublsihed).
[26] A. L. Fetter and J. D. Walecka, *Quantum Theory of Many-Particle Systems* (McGraw-Hill, Boston, 1971).
[27] G. E. Brown and M. Rho, Nucl. Phys. A **372**, 397 (1981).
[28] J. M. VanderKam, G. J. Weisel, and W. Tornow, J. Phys. G: Nucl. Part. Phys. **26**, 1787 (2000).
[29] W. Hauser and H. Feshbach, Phys. Rev. **87**, 366 (1952).
[30] A. J. Koning, S. Hilaire, and M. Duijvestijn, in *Proceedings of the International Conference on Nuclear Data for Science and Technology–ND2007* (EDP Sciences, Paris, 2008), pp. 211–214.
[31] H. F. Arellano, F. A. Brieva, and W. G. Love, Phys. Rev. Lett. **63**, 605 (1989).
[32] R. Crespo, R. C. Johnson, and J. A. Tostevin, Phys. Rev. C **41**, 2257 (1990).
[33] C. Elster, T. Cheon, E. F. Redish, and P. C. Tandy, Phys. Rev. C **41**, 814 (1990).
[34] M. Vorabbi, P. Finelli, and C. Giusti, Phys. Rev. C **93**, 034619 (2016).
[35] G. Hagen and N. Michel, Phys. Rev. C **86**, 021602(R) (2012).
[36] J. Rotureau, P. Danielewicz, G. Hagen, F. M. Nunes, and T. Papenbrock, Phys. Rev. C **95**, 024315 (2017).
[37] A. Idini, C. Barbieri, and P. Navrátil, Phys. Rev. Lett. **123**, 092501 (2019).
[38] J. C. Masson and D. C. Handscomb, *Chebyshev Polynomials* (Chapman & Hall, 2003).
[39] W. H. Press, W. T. Vetterling, S. A. Teukolsky, and B. P. Flannery, *Numerical Recipes in C++*, 2nd ed. (Cambridge University Press, New York, 2002), p. 60.